SCIEPublish

*Article*

# Ethanothermal Synthesis of Dual Emissive Supramolecular Carbon Dots from Naphthalenediol and Quinones with Aggregate Tuned Fluorescence

**Chiyu Wang, Xueying Zhang, Wenhao Fan, Zifan Ye, Manman Zhang and Wenkai Zhang ***

College of Chemistry and Molecular Sciences, Henan University, Kaifeng 475004, China; cywang615@qq.com (C.W.); xueyingzhang111@qq.com (X.Z.); fanwenhao0334@qq.com (W.F.); yezifan0804@163.com (Z.Y.); man-man-zhang@qq.com (M.Z.)

* Corresponding author. E-mail: zhangwenkai@henu.edu.cn (W.Z.)

Received: 20 June 2025; Accepted: 14 August 2025; Available online: 18 August 2025

**ABSTRACT:** Carbon dots (CDs) have attracted considerable interest due to their unique photoluminescence and broad potential in sensing, bioimaging, and optoelectronics. However, precise control of their emission properties through molecular design and understanding of supramolecular aggregation remain challenging. Here, nitrogen-doped carbon dots (H-CDs) with green fluorescence are synthesized via an ethanol-mediated solvothermal method using 1,3-dihydroxynaphthalene as a rigid π-conjugated carbon source and 2,3-dichloro-5,6-dicyano-p-benzoquinone (DDQ) as both oxidant and nitrogen donor. The synthesis involves complex molecular transformations yielding amorphous supramolecular carbon dots stabilized mainly by noncovalent interactions. Characterization confirmed abundant oxygen- and nitrogen-containing functional groups and an amorphous structure devoid of crystalline residues. Hierarchical H-type aggregation driven by π-π stacking and hydrogen bonding governs the photophysical behavior of the H-CDs, inducing a concentration-dependent evolution from blue-emitting monomers to green-emitting supra-CDs, accompanied by particle growth, red-shifts in the emission spectrum, and a pronounced elongation of the fluorescence lifetime. Temperature- and salt-dependent studies reveal that emission intensity increases with rising temperature and low ionic strength, due to distorted H′-aggregates with weak excitonic coupling and electrostatic screening of surface charges. These insights deepen the understanding of structure-property relationships in carbon dots and offer guidance for tailoring their photophysical properties for advanced optoelectronic applications.

**Keywords:** Nitrogen-doped carbon dots; Supramolecular aggregation; Photoluminescence; Fluorescence lifetime; π–π stacking



## 1. Introduction

In the past decade, a new exciting class of metal-free and carbon-rich photoluminescent (PL) nanomaterials, carbon dots (CDs), has been developed as a promising functional component in bioimaging, sensors, photocatalysts, and optoelectronic devices [1,2]. Various approaches have been developed to fabricate CDs, including “top-down” and “bottom-up” methods. Compared with top-down derived CDs [3–5], the bottom-up derived CDs, which are mainly prepared through dehydration, condensation, polymerization and carbonization of organic precursors, exhibit distinctive advantages including high PL quantum yield (QY) [6,7], large-scale synthesis [8], emission color tuning [9–11], multi-element doping [12,13]. Citric acid has been one of the most frequently used precursors for synthesizing CDs through bottom-up carbonization routes due to the direct process and high PLQY [14,15]. Inspired by the citric acid methodology, other organic precursors with definite chemical structures are explored to synthesize multicolor CDs, such as phenylenediamines [10], chloroform/diethylamine [11], diaminobenzenesulfonic acid [16], and trinitropyrene [17]. Nevertheless, it is highly desirable and a great challenge to establish a new and extendable synthesis methodology for multicolor CDs covering the entire visible region, especially long wavelength light emission [18–23].

Another important issue is that, for most of the bottom-up CDs, a complete characterization of their structural and chemical properties is still lacking, making the possible PL origins debatable, which then lead to several hypotheses including $sp^2$ cluster [24–26], surface state [27–30], charged nitrogen and molecular states [31,32]. Highly

https://doi.org/10.70322/gct.2025.10013

photoluminescent molecules have been frequently reported as the main PL origins in bottom-up pathways to CDs [33–35]. For example, in citric acid derived CDs, the 2-pyridone compound has been separated and proved to be the sole PL origin [36,37]. These CDs are characterized as fluorophore dominating and lack a carbon lattice, exhibiting analogous PL properties as those carbogenic or graphene dots, including excitation dependent and large Stokes shift emission [38,39]. To explain the unique PL properties of amorphous CDs, the viewpoint of supramolecular aggregation is frequently proposed. For citric acid derived CDs, the molecular fluorophore is found to self-assemble into amorphous aggregates through hydrophobic interaction and $\pi$-$\pi^*$ stacking [40,41]. By means of liquid chromatography-tandem mass spectrometry, citric acid derived CDs are disclosed to exist as supramolecular clusters with their individual monomer units linked together through noncovalent bonding forces [42–44]. In analogy with dye aggregation, both J-type and H-type aggregates have also been suggested in citric-acid-based CDs [45–47], and the exciton model is used to explain the large Stokes shift of CDs' PL [48]. The strong support of the idea of considering CDs as H-type aggregate emitters has been found in the results of experiments on single nanoparticles [49,50] and cryogenic studies [51]. Meanwhile, weakly coupled H-aggregate looks like J-aggregate due to the exciton-lattice interaction, which was independently found in amorphous CDs by two groups. Compared with the collective explanation for the origin of PL in CDs, such as core and surface states, the viewpoint of supramolecular aggregation provides more definitive evidence for fundamental ambiguities regarding the photoluminescence of CDs, which should be adapted to a wider range of CDs materials, not limited to citric acid derived CDs. In CDs, phenomena like aggregation-induced emission (AIE) have been reported, specifically aggregation-induced fluorescence enhancement and aggregation-induced wavelength-redshifts. To a large degree, concentration-dependent PL reflects AIE in CDs. Many researchers have proposed that aggregation increases the conjugation degree of surface luminophores, leading to a decrease in band gap. Hence, emission wavelengths gradually red shift with increasing CDs concentration [52]. Yang et al. synthesized hydrophobic N, S-doped CDs (H-CDs) via a one-pot solvothermal method using melamine (MA) and dithiosalicylic acid (DTSA)/acetic acid solution. The H-CDs display dual-switch mode luminescence between blue dissolved fluorescence and red AIE [53]. Wang et al. used phloroglucinol and urea as sources, and by adjusting the reactant ratio and microwave power, prepared four typical CDs, emitting green (G-CD), yellow (Y-CD), orange (O-CD), and red fluorescence (R-CD) in a one-step microwave method [54].

This work explored a new synthetic method using 1,3-dihydroxynaphthalene/2,3-dichloro-5,6-dicyano-*p*-benzoquinone (DDQ) as precursors and ethanol-mediated solvothermal synthesis to produce amorphous carbon dots (CDs) with green fluorescence. Due to the low reaction temperature (mainly under 200 °C) and the presence of an oxidant, the diphenols are unlikely to experience carbonization to form CDs with a clear carbon lattice [55], thus only supramolecular aggregates are generated. Through concentration- and temperature-dependent spectroscopy, strong H-type and weakly coupled H′-type aggregates were identified in the green CDs [56]. Subsequently, the salt effect induced a transformation in the PL spectra and morphology between H-type and H′-type aggregates.

## 2. Materials and Methods

### *2.1. Materials*

1,3-dihydroxynaphthalene (≥98%) and DDQ (≥98%) were purchased from Aladdin (Shanghai, China). Ethanol (analytical grade), dichloromethane (DCM), and methanol were obtained from Sinopharm Chemical Reagent Co., Ltd., Shanghai, China. All reagents were used as received without further purification.

### *2.2. Synthesis of CDs*

H-CDs were synthesized via an ethanol-mediated solvothermal reaction using 1,3-dihydroxynaphthalene as the diphenol precursor and DDQ as the oxidant, following a modified procedure based on previous reports [19]. Briefly, 0.16 g (1.0 mmol) of 1,3-dihydroxynaphthalene and 0.57 g (2.5 mmol) of DDQ were dissolved in 15 mL of ethanol under ultrasonic agitation to form a clear solution. The mixture was transferred into a Teflon-lined stainless steel autoclave, sealed, and heated at 180 °C for 4 h. After naturally cooling to room temperature, the reaction mixture was subjected to purification by silica gel column chromatography using dichloromethane/methanol mixtures with gradient elution ratios (50:1, 30:1, 20:1, and 10:1, *v*/*v*). The fraction eluted at a 10:1 DCM/methanol ratio was collected, and the solvent was removed under reduced pressure using a rotary evaporator to yield H-CDs as a dark solid. The isolated yield was approximately 27% by weight.

### *2.3. Characterization*

Atomic force microscopy (AFM) images were acquired in tapping mode under ambient conditions using a Dimension Icon system (Bruker, Billerica, MA, USA) on freshly cleaved mica substrates. Transmission electron microscopy (TEM) was performed on a JEM-1200EX instrument (JEOL, Tokyo, Japan) operated at 120 kV. Fourier-transform infrared (FTIR) spectra were recorded using a Bruker Vertex 70 spectrometer (Bruker, Billerica, MA, USA). Proton nuclear magnetic resonance ($^1$H NMR) spectra were obtained on a Bruker AVANCE 400 MHz spectrometer (Bruker, Billerica, MA, USA). X-ray diffraction (XRD) patterns were collected in reflection mode using a Bruker D8 Advance diffractometer with Cu Kα radiation (λ = 0.15418 nm) (Bruker, Billerica, MA, USA). Dark-field optical scattering images were captured using an RTS2-HU-DZX microscope (Zolix, Beijing, China) equipped with a 50× objective (NA = 0.8) and a CMOS image sensor (900 × 600 pixels). Particle size distribution was analyzed using dynamic light scattering (DLS) on a Nano ZS90 laser particle size analyzer (Malvern Instruments, Malvern, UK). UV–vis absorption spectra were measured on a Hitachi U-4100 spectrophotometer (Tokyo, Japan). Photographs of fluorescence emission under 365 nm UV illumination (ZF-8D lamp) were taken using a Nikon D7200 digital camera. Steady-state photoluminescence (PL) spectra were recorded using a Hitachi F-7000 fluorescence spectrophotometer (Tokyo, Japan). Time-resolved PL decay curves were measured via time-correlated single photon counting (TCSPC), using a picosecond pulsed diode laser as the excitation source (pulse width: 868.3 ps; wavelength: 369.4 nm; bandwidth: 12.8 nm; repetition rate: 5 MHz).

## 3. Results and Discussion

As illustrated in Scheme 1, nitrogen-doped, green-fluorescent CDs bearing amino and hydroxyl surface groups were synthesized via an ethanol-mediated solvothermal method. The reaction employed 1,3-dihydroxynaphthalene as a rigid, π-conjugated aromatic carbon source and DDQ as a dual-function reagent, serving both as an oxidant (via its quinone moiety) and a nitrogen donor (via its cyano groups), in a molar ratio of 1:2.5. The formation process involves several key stages: (1) DDQ abstracts phenolic hydrogen atoms from 1,3-dihydroxynaphthalene, leading to its reduction to $DDQH_2$ and the formation of phenoxy radicals. This promotes π-π stacking and molecular aggregation through radical coupling and hydrogen bonding; (2) Under high-temperature ethanol conditions, the cyano groups of DDQ undergo nucleophilic addition, followed by rearrangement and hydrolysis to yield carboxyl or amide functionalities. Alternatively, alcoholysis may generate imine esters that subsequently hydrolyze into primary amides, contributing to nitrogen doping; (3) The resulting hydroxyl, carboxyl, and amino groups participate in dehydration-condensation reactions, forming a molecularly cross-linked network. (4) Progressive aromatization and partial carbonization result in the formation of supramolecular carbon dots, stabilized by noncovalent interactions rather than graphitized cores. When ethanol is used as the solvent, the final H-CD solution appears brown under white light and emits green fluorescence, consistent with the formation of emissive molecular aggregates.

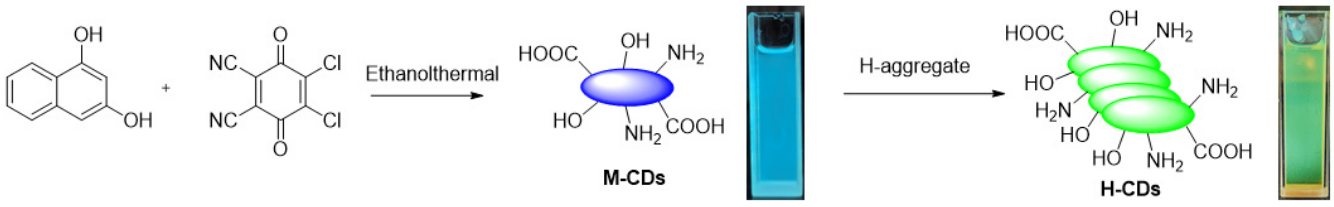


**Scheme 1.** Schematic illustration of the ethanothermal synthesis of fluorescent CDs. Photographs on the right show the resulting CD solutions under white light (**left**) and 365 nm UV light (**right**), with ethanol as the solvent.

As shown in Figure 1a, TEM images reveal the presence of supramolecular nanodots alongside typical carbon nanodots. The concentration of the sample used for testing TEM is $10^{-4}$ mg/mL, which can prevent aggregation. Size analysis from TEM indicates an average particle diameter of 17.8 nm with a standard deviation of 7.4 nm. AFM was employed for the first time to characterize the morphology of the CDs (Figure 1b). A methanol solution of CDs was drop-cast onto freshly cleaved mica and dried at room temperature, enabling self-assembly. Discrete nanostructures were observed across all samples, with minor variations in height and distribution. AFM height profiles (Figure 1c) indicate that individual carbon dots are typically 5–8 nm in height, generally smaller than 10 nm, while aggregates exceed 25 nm. These observations support the notion that the CDs exist as supramolecular aggregates or self-assembled

nanostructures. The abundant surface functional groups likely promote extensive hydrogen bonding, contributing to the formation of amorphous, supramolecular aggregates.

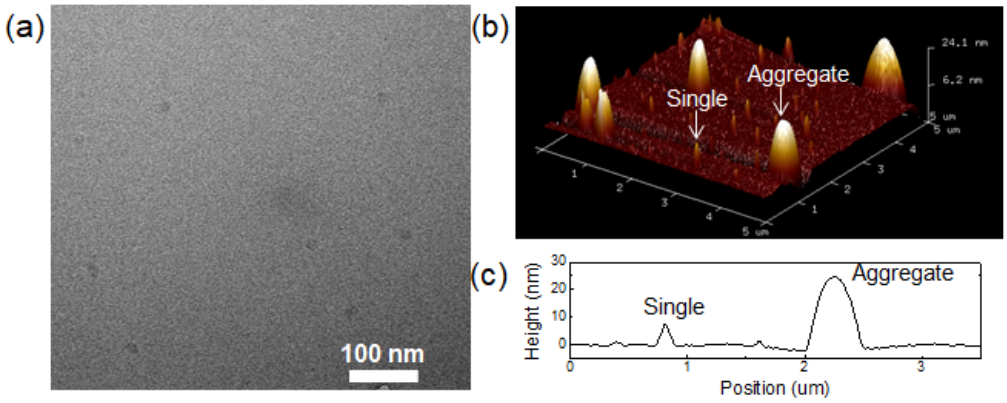


**Figure 1.** (**a**) Transmission electron microscopy (TEM) images of H-CDs. (**b**) AFM images of H-CDs with individual carbon dots and aggregates are indicated. (**c**) Height profiles corresponding to the selected particles are marked in panel (**b**).

The FT-IR spectrum of H-CDs (Figure 2a) displays abundant oxygen-containing functional groups, including hydroxyl (–OH, 3212 $cm^{-1}$), carbonyl (C=O, 1705 $cm^{-1}$), cyano groups (C≡N, 2251 $cm^{-1}$), and ether (C–O, 1192 $cm^{-1}$) vibrations. The sharp and intense vibrational band observed at approximately 2200–2260 $cm^{-1}$ in the FT-IR spectrum is characteristic of the C≡N stretching vibration. This signal strongly corresponds to the cyano (-C≡N) functional groups present in the DDQ structure. These results suggest that the CDs derived from the diphenol/oxidant system consist of π-conjugated heterocyclic frameworks bearing various oxygen-containing moieties such as carboxyl, hydroxyl, ester, ether, and aldehyde groups. The presence, abundance, and spatial distribution of these groups are believed to play critical roles in the supramolecular self-assembly and multicolor emission properties of the CDs. XRD analysis of solid-state H-CDs (Figure 2b) reveals a broad, diffuse peak centered at 2θ = 22.8°, characteristic of an amorphous structure. The absence of sharp diffraction peaks confirms the lack of long-range crystalline order. Notably, no crystalline signatures corresponding to unreacted molecular precursors (e.g., 1,3-dihydroxynaphthalene or DDQ) or byproducts were detected, which would typically exhibit distinct sharp peaks. These findings confirm that the hydrothermally synthesized and purified H-CDs are amorphous carbon nanodots with disordered internal structure, consistent with common solution-processed carbon dots and distinct from crystalline molecular species. The $^{1}$H NMR spectrum of H-CDs (Figure 2c) exhibits broad signals indicative of heterogeneous chemical environments, in line with the formation of amorphous carbon nanodots. A downfield resonance at δ = 11.6 ppm is assigned to carboxylic acid protons (–COOH) involved in face-to-face π-stacked aggregates, while the signal at δ = 10.5 ppm is attributed to phenolic hydroxyl protons (Ar–OH) located at hydrogen-bonding interfaces. The peak at δ = 6.40 ppm is assigned to the aromatic proton of an enolized β-diketone structure (–C=C–OH), where intramolecular hydrogen bonding creates a pseudo-aromatic system. This chemical shift is characteristic of enol tautomers in conjugated systems. Meanwhile, the signal at δ = 4.25 ppm corresponds to benzylic methylene protons (–$CH_2$–O–Ph) formed through nucleophilic addition between carbonyl intermediates and phenolic moieties during microwave-assisted carbonization. The overall broadening of these resonances reflects the complex, disordered nature of the CDs and further supports the exclusion of residual crystalline molecular species after purification by column chromatography.

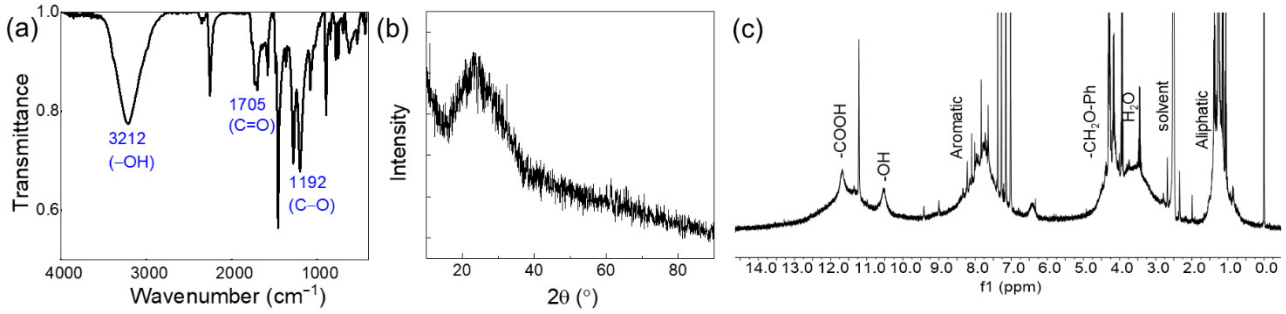


**Figure 2.** (**a**) FT-IR spectrum of H-CDs.; (**b**) XRD patterns of H-CDs; (**c**) $^{1}$H-NMR (400 MHz, DMSO-$d_6$) spectrum of H-CDs.

As shown in Figure 3, the particle sizes of H-CDs at concentrations of $10^{-3}$, $10^{-2}$, $10^{-1}$, and 1 mg/mL were measured to be approximately 0.27 μm, 0.60 μm, 1.27 μm, and 2.06 μm, respectively, using a laser particle size analyzer. Notably, relatively large particle sizes were observed even at low concentrations, suggesting the presence of stable aggregates rather than isolated nanodots. This phenomenon is attributed to a hierarchical assembly process driven by H-type aggregation. Specifically, the H-CDs possess abundant π-conjugated domains and polar functional groups, enabling π–π stacking and hydrogen bonding interactions that promote the formation of nanoscale aggregates (~0.27 μm) even at dilute concentrations. These primary aggregates are responsible for the blue fluorescence observed at low concentrations. Upon increasing the concentration, these nanoscale aggregates further assemble into larger supraparticles through directional H-type stacking, characterized by face-to-face π–π interactions. This higher-order aggregation leads to extended structures with increased particle size and a concomitant red-shift in fluorescence emission from blue to green.

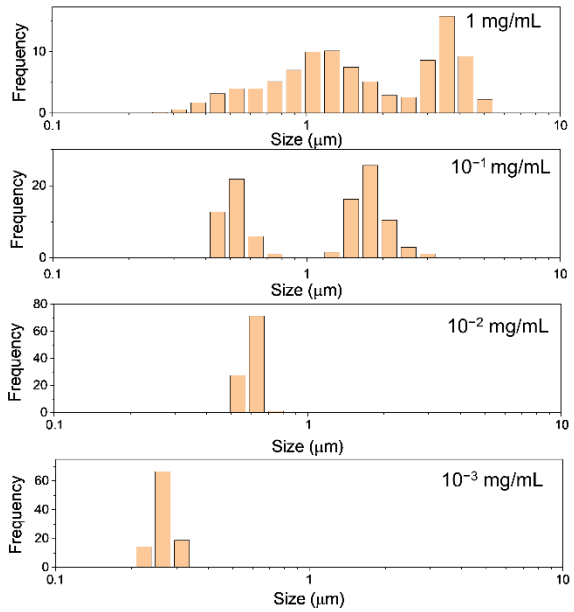


**Figure 3.** Particle size distribution histograms of H-CDs at different concentrations measured by laser particle size analyzer. From bottom to top: $10^{-3}$ mg/mL, $10^{-2}$ mg/mL, $10^{-1}$ mg/mL, and 1 mg/mL.

Figure 4 reveals distinct concentration-dependent morphological transitions of H-CDs as observed under dark-field optical microscopy. The H-CDs exhibit a fine, well-dispersed distribution characterized by discrete nanoscale particulates at a low concentration of $10^{-3}$ mg/mL (Figure 4a). These are interpreted as monomeric or small supramolecular assemblies of carbon dots, stabilized by relatively weak intermolecular forces such as hydrogen bonding and π-π interactions. The uniformity and isolation of the particles at this concentration suggest minimal aggregation, enabling the retention of individual dot-like features and resulting in consistent blue photoluminescence under UV illumination. In stark contrast, when the concentration is increased to 1 mg/mL (Figure 4b), the morphology shifts dramatically toward the formation of large, micron-sized aggregates with complex clustered structures. These aggregates indicate a hierarchical H-type assembly process, driven by intensified intermolecular interactions due to the increased proximity of particles in solution. Specifically, the π-conjugated domains of the carbon dots facilitate directional face-to-face stacking (characteristic of H-aggregation), which promotes anisotropic growth of the assemblies. Additionally, the presence of abundant polar functional groups (e.g., hydroxyl, carboxyl, and amine groups) likely contributes to forming a dynamic hydrogen bonding network, further stabilizing these higher-order structures. This transition from monodisperse particles to large hierarchical assemblies illustrates a delicate balance between concentration, molecular interactions, and colloidal stability. At lower concentrations, entropic factors and solvent interactions dominate, favoring dispersion. At higher concentrations, enthalpic contributions from noncovalent interactions overcome dispersion forces, leading to spontaneous self-organization into larger structures. These morphological changes are also accompanied by optical property evolution, such as a red-shift in emission from blue to green, highlighting the interplay between structural organization and photophysical behavior.

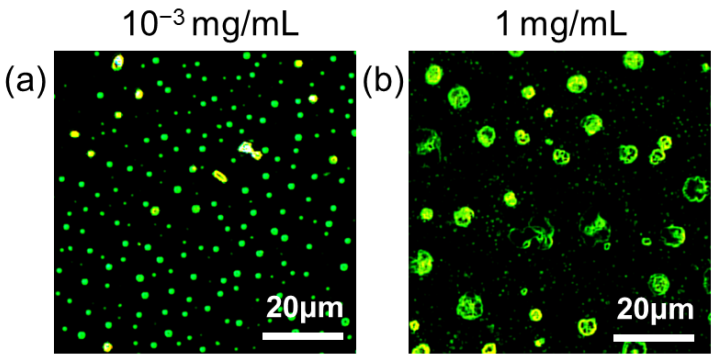


**Figure 4.** Dark-field optical micrographs of H-CDs prepared at concentrations of (**a**) $10^{-3}$ mg/mL and (**b**) 1 mg/mL.

Continuing with the assumption that H-CDs tend to form H-type aggregates upon increasing concentration, a detailed comparative analysis of their absorption and PL excitation spectra was conducted. As shown in Figure 5a, the UV-vis absorption spectra of H-CDs evolve significantly with increasing concentration. In comparison with the monomeric CDs (M-CDs), two new absorption bands emerge, exhibiting opposite spectral shifts: the absorption peak at ~395 nm gradually blueshifts to ~370 nm, while the peak at ~318 nm red-shifts to ~330 nm (Figure 5b). Drawing on classical excitonic models of dye aggregation [57,58], the blue-shifted band can be attributed to the formation of ordered H-aggregates, characterized by excitonic coupling with a side-by-side geometry. In contrast, the red-shifted band is ascribed to a locally distorted H′-aggregate, in which structural disorder or excitonic relaxation causes a J-aggregate-like red-shift. Further insights are provided by the PL excitation spectra. When monitored at 450 nm (corresponding to blue emission), the excitation spectrum exhibits a narrow peak at 353 nm with a shoulder around 400 nm (Figure 5c). However, when monitored at 530 nm (green emission), the excitation spectrum shows a more complex structure: the 353 nm peak splits into two peaks centered at 330 nm and 367 nm, while the shoulder around 410 nm shifts further to ~450 nm (Figure 5d). These spectral changes suggest distinct excitation pathways and stronger coupling effects at higher concentrations, consistent with the emergence of H′-aggregates. The splitting and red-shift of excitation bands further support the role of structural relaxation and local symmetry breaking within the aggregated states. It is also noteworthy that the H-CDs exhibit a large Stokes shift, exceeding 250 nm. Such a shift could be associated with aggregation-induced emission behavior, wherein emission originates from states stabilized through interparticle interactions or suppressed nonradiative decay in the aggregated phase. A closer comparison between the concentration-dependent excitation and absorption spectra (Figures 5c,d) reveals substantial differences in both spectral shape and position, reinforcing the distinct nature of the emitting and absorbing species. For example, the main excitation band was monitored at 450 nm, shifting from 380 nm to 354 nm with increasing concentration, while that was monitored at 530 nm with red-shifts from 327 nm to 332 nm. Concurrently, the relative intensity of the monomer-associated features at longer wavelengths decreases dramatically, indicating a progressive suppression of isolated species and dominance of aggregated states in the photophysical behavior.

As shown in Figure 6, three-dimensional fluorescence spectroscopy was used to investigate the excitation-emission behavior of H-CDs in ethanol across four concentrations ranging from 0.001 to 1 mg/mL. At low concentrations (0.001–0.01 mg/mL, Figure 6a,b), the fluorescence spectra exhibit dual emission centers centered around 460 nm when excited at approximately 249 nm and 398 nm, corresponding to emission from well-dispersed individual carbon dots. When the concentration reaches a critical threshold of 0.1 mg/mL (Figure 6c), a pronounced red-shift occurs: the dominant emission peak shifts to 517 nm (excited at 385 nm), with a much stronger intensity compared to a weaker residual blue-shifted peak at 455 nm (excited at 334 nm). At the highest concentration studied (1 mg/mL, Figure 6d), the dual emission centers further differentiate into peaks at 500 nm (excited at 443 nm) and 520 nm (excited at 410 nm), with the 500 nm peak becoming dominant. These spectral changes clearly demonstrate a concentration-dependent red-shift transition in the dominant emission, progressing from ~460 nm at low concentration (0.001 mg/mL), to 517 nm at the critical concentration (0.1 mg/mL), and a split emission at 500/520 nm at the highest concentration (1 mg/mL). The observed ~57 nm red-shift jump at 0.1 mg/mL marks a critical point in the aggregation behavior of H-CDs. Mechanistically, H-CDs are predominantly dispersed monomer-like species below this critical concentration, emitting characteristic blue fluorescence. As concentration increases, π–π interactions induce face-to-face stacking, leading to the formation of tetrameric H-aggregates. This aggregation modifies the electronic structure by contracting the energy gap, which results in a substantial red-shift in emission wavelength and an intensity redistribution favoring longer wavelengths.

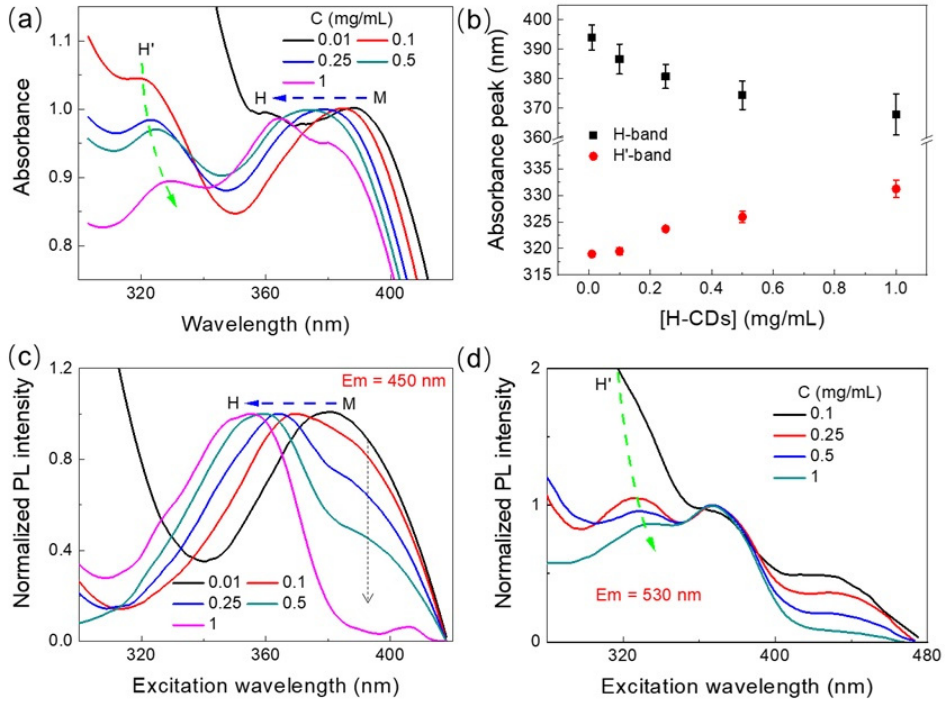


**Figure 5.** (**a**) Changes in the UV-vis absorbance spectra of H-CDs with increasing solution concentration. The blue and green dashed arrows indicate the blue-shifted H-band and red-shifted H′-band, respectively. The M denotes the spectral position of the monomeric (dispersed) H-CDs, while H refers to the spectral features arising from interparticle aggregation. (**b**) Concentration-dependent spectral shifts of the H-band and H′-band. (**c**,**d**) Excitation spectra of H-CDs at different concentrations, monitored at emission wavelengths of $\lambda_{em}$ = 450 nm (**c**) and $\lambda_{em}$ = 530 nm (**d**). The PL excitation spectra are carried out to minimize inner filter effects using a low-volume cuvette (1 × 4 mm, 140 µL). All dotted arrows indicate the direction of concentration increasing from 0.01 mg/mL to 1 mg/mL.

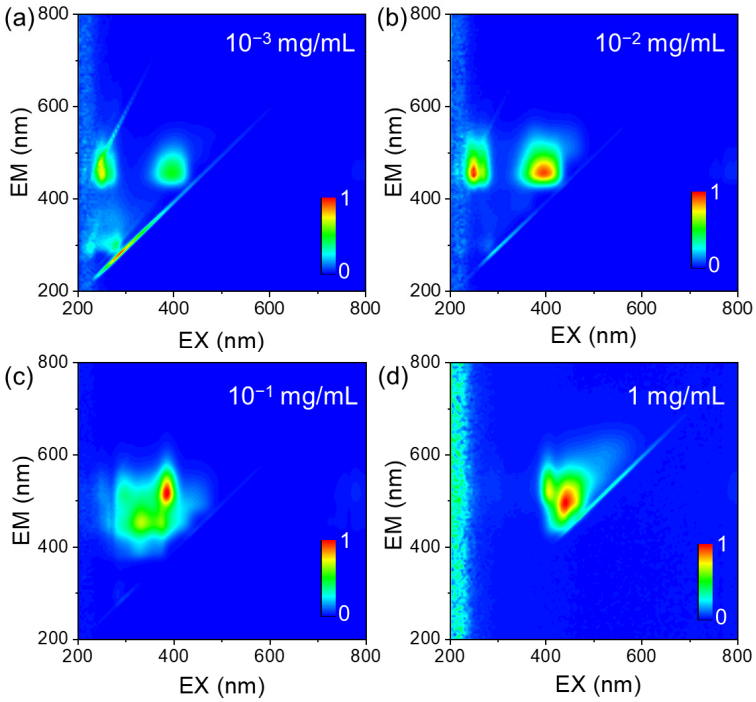


**Figure 6.** Three-dimensional fluorescence spectra of H-CDs solutions at varying concentrations. (**a**) $10^{-3}$ mg/mL, (**b**) $10^{-2}$ mg/mL, (**c**) $10^{-1}$ mg/mL, (**d**) 1 mg/mL.

As discussed earlier, the diphenol/oxidant-derived H-CDs consist of supramolecular aggregates whose morphology and PL properties strongly influence their aggregation state [56,57]. We studied how the PL emission spectra change with solution concentration by diluting a concentrated sample stepwise. Figure 7a presents the fluorescence emission

spectra at various concentrations, while Figure 7b shows the normalized spectra highlighting the evolution of emission peaks. As the H-CD concentration decreases, the dominant emission peak gradually shifts from approximately 520 nm to 450 nm, indicating a transition from aggregated to more dispersed states. Figure 7c plots the fluorescence intensity ratio ($I_{520}/I_{450}$) versus concentration, revealing a clear concentration-dependent increase in the relative contribution of the red-shifted emission band. At low concentrations (<0.01 mg/mL), the H-CDs mainly exist as dispersed or loosely associated species, emitting strongly around 450 nm. This emission is attributed to intrinsic electronic transitions of the individual carbon dot units or small oligomers. Above a critical concentration (~0.1 mg/mL), increased molecular packing via face-to-face π-π stacking leads to the formation of ordered H-aggregates, altering the electronic environment and resulting in a dominant emission band near 520 nm. The observed red-shift of emission with aggregation contrasts with classical H-aggregate models that typically predict a blue shift. This discrepancy suggests aggregation induces a rearrangement in molecular packing and electronic coupling within the H-CDs, leading to new emissive states. Thus, the concentration-dependent PL changes reflect a dynamic equilibrium between dispersed and aggregated forms of H-CDs, where supramolecular assembly modulates their optical properties.

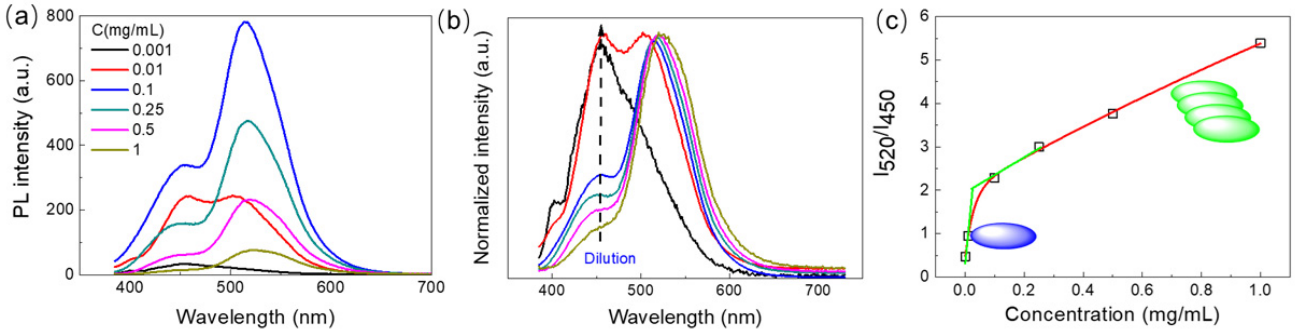


**Figure 7.** (**a**) Fluorescence emission spectra of H-CDs in ethanol solution at varying concentrations. (**b**) Normalized fluorescence emission spectra of aqueous H-CDs solutions at different dilution levels. The arrows indicate increasing dilution times; the original concentration of pristine H-CDs is approximately 1 mg/mL. (**c**) Plot of the fluorescence intensity ratio ($I_{520}/I_{450}$) of H-CDs as a function of concentration, illustrating the concentration-dependent emission shift. Red line: added trend. Green lines: tangents for two concentration ranges, indicating critical aggregation concentration. Blue ellipsoids: individual CDs. Green stacked ellipsoids: aggregated CDs.

As shown in Figure 8, time-resolved fluorescence decay profiles of H-CDs were investigated under 375 nm picosecond pulsed laser excitation across four concentrations (0.001–1 mg/mL). Emission was monitored at 450 nm for dilute samples (0.001 and 0.01 mg/mL, blue emission) and at 525 nm for more concentrated ones (0.1 and 1 mg/mL, green emission). All decay curves were fitted using a biexponential model described by the equation $I(t) \sim B_1 exp(-t/\tau_1) + B_2 exp(-t/\tau_2)$, where $\tau_1$ and $\tau_2$ represent the fast and slow lifetime components, respectively, and $B_1$, $B_2$ are their amplitude contributions.

As shown in Table 1, the lifetime data strongly support the interpretation of emission origin shifting from monomers to aggregates as concentration increases. At low concentrations (0.001 and 0.01 mg/mL), where emission is centered at 450 nm, the decay behavior is biexponential with a dominant long-lived component (~8.8 ns) and a small fast component (~0.4 ns), reflecting a mixture of monomer-like emissive states and minor aggregation or surface-state contributions. As the concentration increases to 0.1 mg/mL, the emission red-shifts to 525 nm and the decay becomes dominated by the long component (10.73 ns), with the short component nearly vanishing. At 1 mg/mL, the decay is essentially single-exponential with a lifetime of 11.31 ns, indicating a highly uniform emissive environment consistent with compact, ordered aggregates. This excellent agreement between emission wavelength shift and fluorescence lifetime evolution clearly confirms that the concentration-dependent optical properties arise from a well-defined transition from isolated monomeric CDs to emissive aggregates with suppressed nonradiative decay channels [59–61].

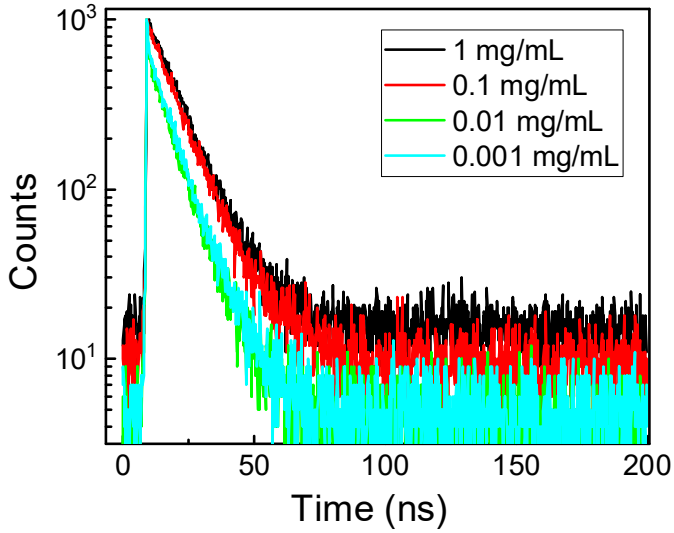


**Figure 8.** Fluorescence decay curve of H-CDs in ethanol solutions at different concentrations.

**Table 1.** Fluorescence lifetime fitting parameters of H-CDs in ethanol at different concentrations.

| C (mg/mL) | $\lambda_{em}$ (nm) | $\tau_1$ (ns) | $B_1$ (%) | $\tau_2$ (ns) | $B_2$ (%) | $\tau_{ave}$ (ns) | $\chi^2$ |
|---|---|---|---|---|---|---|---|
| $10^{-3}$ | 450 | 0.40 | 38.48 | 8.82 | 61.52 | 8.59 | 0.996 |
| $10^{-2}$ | 450 | 0.40 | 38.48 | 8.82 | 61.52 | 8.59 | 0.996 |
| $10^{-1}$ | 525 | 0.37 | 4.99 | 10.73 | 95.01 | 10.71 | 0.997 |
| 1 | 525 | 11.31 | 100 | - | - | 11.31 | 0.996 |

Note: $\tau_1$ and $\tau_2$ represent the short and long lifetime components, respectively. $B_1$ and $B_2$ denote their relative amplitude contributions. $\tau_{ave}$ is the amplitude-weighted average lifetime. The emission wavelength ($\lambda_{em}$) and lifetime components indicate a clear concentration-dependent shift in emission and decay behavior, associated with monomer-to-aggregate transitions.

According to Kasha's exciton theory [62], weakly emissive H-aggregates are characterized by a blue-shifted excitation or absorption band, whereas highly emissive J-aggregates exhibit a red-shifted excitation or absorption feature. Based on these classical models, one may reasonably associate blue-shifted excitation/absorption bands with H-aggregates and red-shifted ones with J-aggregates. However, such a binary classification becomes inadequate for more structurally complex aggregates, especially when the excitation/absorption and emission spectra exhibit clear vibronic progressions. To address this complexity, Spano introduced a more refined model based on excitonic coupling strength, providing critical insights into the identification of H- and J-type aggregates [63,64]. In the present study, by extending Spano's criteria, we performed temperature-dependent PL measurements at the respective excitation maxima of the blue- and red-shifted bands. The fluorescence intensity increases with temperature for the weakly blue-emissive state, consistent with H-aggregate behavior (Figure 9a). One might initially assume a J-aggregate character for the red-shifted excitation associated with green emission, anticipating a pronounced intensity decrease with rising temperature due to exciton-phonon interactions. However, we observe an increase in emission intensity with temperature (Figure 9b), a feature more consistent with H-aggregates rather than J-aggregates. Thus, we do not attribute this red-shifted excitation to a J-aggregate but rather assign it to a distorted or weakly coupled H′-aggregate. This anomalous low-energy H′-aggregate excitation likely arises from a combination of weak excitonic coupling and structural disorder, such as increased interparticle distances and suboptimal spatial configurations among the CDs. These structural features relax the otherwise forbidden lower-energy excitonic transitions, giving rise to the red-shifted excitation band.

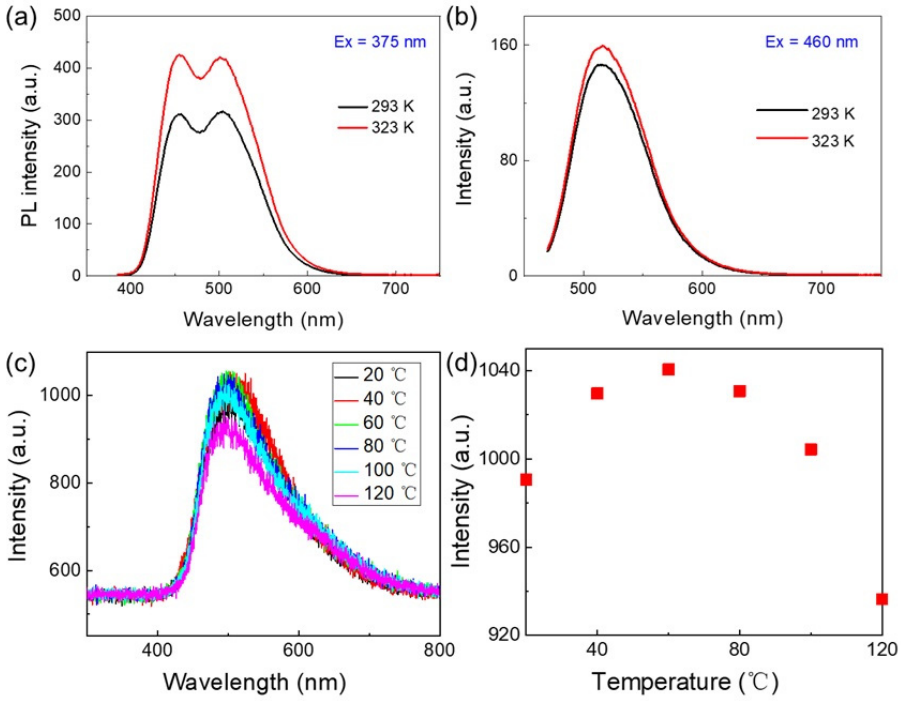


**Figure 9.** (**a**) Effect of increasing temperature on the emission spectra of H-CDs (C = 0.25 mg/mL) measured with excitation wavelengths at 375 nm. (**b**) Effect of increasing temperature on the emission spectra of H-CDs (C = 0.25 mg/mL) was measured with excitation wavelengths of 450 nm. (**c**) Fluorescence emission spectroscopy of H-CDs at different temperatures (20–120 °C). (**d**) The variation of fluorescence intensity of H-CDs with temperature.

As illustrated in Figure 9c,d, we systematically evaluated the fluorescence intensity of H-CDs across a temperature range from 20 to 120 °C. The emission intensity initially increased with temperature, peaking before gradually declining. Specifically, the fluorescence intensity gradually increased from room temperature up to 60 °C, reaching its peak at this point. Beyond 60 °C, the intensity steadily declined as the temperature continued to rise, indicating a clear temperature-dependent modulation of fluorescence behavior. This systematic variation confirms that temperature plays a regulatory role in the photophysical behavior of H-CDs, strongly associated with their aggregation state. At lower temperatures, carbon dots exist primarily as monomers with limited intermolecular interactions, where excitation energy is dissipated mainly through nonradiative decay, resulting in relatively weak fluorescence. Increased molecular motion facilitates H-aggregate formation as the temperature rises, enhancing π–π stacking and hydrogen bonding interactions. These interactions constrain intramolecular rotations and vibrations, suppressing nonradiative pathways and promoting radiative emission. The fluorescence reaches its optimum at 60 °C, indicating an ideal aggregation state. Beyond this temperature, thermal agitation disrupts the aggregate's structural order, weakening intermolecular interactions or introducing enhanced local charge-transfer processes, which leads to fluorescence quenching. Additionally, the formation of H-aggregates is often accompanied by a red shift in emission wavelength, such as the observed transition from blue to green emission. The dynamic modulation of aggregation stability with temperature thus provides a compelling explanation for the initial increase followed by a decrease in fluorescence intensity.

Fluorescence spectra of CD solutions were measured under varying concentrations of sodium chloride (NaCl) and potassium chloride (KCl) at 5, 20, and 50 mmol/L, while keeping all other conditions constant. As shown in Figure 10a,b, increasing the concentration of either salt within this low-to-moderate ionic strength range leads to a pronounced enhancement of the CDs' fluorescence intensity. This effect can be primarily attributed to the electrostatic screening of the negatively charged CD surfaces by $Na^+$ or $K^+$ ions. In aqueous media, the surface carboxyl groups (-COOH) ionize to $–COO^–$, imparting significant negative charge and generating a strong electrostatic field that can disrupt the CDs' electronic structure or facilitate nonradiative recombination pathways, thus lowering fluorescence quantum yield. The addition of $Na^+$ or $K^+$ forms an electrical double layer around the CDs, effectively neutralizing this surface charge and reducing interference with radiative recombination. It is worth noting that although the hydration radii of $Na^+$ and $K^+$ are different, the almost identical fluorescence enhancement observed provides strong evidence for this charge screening mechanism, as these two cations have the same charge state and electrostatic function. This screening suppresses nonradiative relaxation channels, thereby enhancing fluorescence emission. Additionally, binding of these cations to

surface –$COO^-$ groups diminishes their electron-withdrawing effect, which weakens the intramolecular charge transfer (ICT) between electron-donating groups (such as amino or hydroxyl) and electron-accepting carboxyl groups. This disruption inhibits the nonradiative ICT relaxation pathway, further favoring radiative recombination within the CDs. The elevated ionic strength may also modify the solvation shell around the CDs, restricting molecular vibrations or rotations that typically dissipate energy non-radiatively. Moreover, salt-induced weak interparticle interactions, such as ion bridging, may restrict the motion of surface functional groups, thereby activating weak aggregation-induced emission behavior. It is important to note that this enhancement occurs within a critical ionic concentration window (5–50 mmol/L) where electrostatic screening and weak aggregation dominate; higher ionic strengths could lead to aggregation-caused quenching, reversing the fluorescence enhancement.

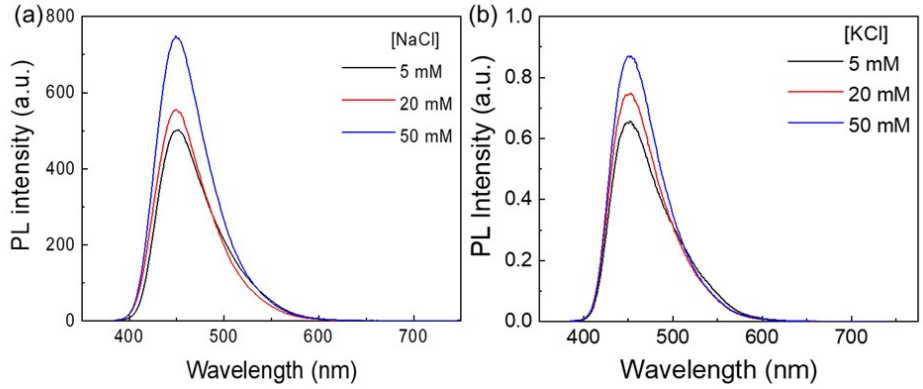


**Figure 10.** (**a**) Photoluminescence emission spectra of H-CDs excited at 375 nm in the presence of varying concentrations of NaCl. (**b**) Photoluminescence emission spectra of H-CDs excited at 375 nm with different concentrations of KCl.

## 4. Conclusions

In summary, nitrogen-doped carbon dots (H-CDs) with green fluorescence were successfully synthesized via a solvothermal approach using a rigid π-conjugated carbon source and a multifunctional oxidant/nitrogen donor. The resulting amorphous supramolecular carbon dots are stabilized primarily by noncovalent interactions, featuring abundant oxygen- and nitrogen-containing surface groups. Hierarchical H-type aggregation strongly influences their photophysical properties, which drives a concentration-dependent transition from blue-emitting monomers to green-emitting supra-CDs, accompanied by significant particle growth and fluorescence lifetime elongation. Temperature- and salt-dependent experiments further elucidate the role of distorted H′-aggregates, electrostatic effects, and molecular dynamics in modulating emission intensity. These findings provide valuable insights into the structure–property relationships of carbon dots and highlight strategies for precise tuning of their emission through supramolecular assembly and environmental control, advancing their potential in optoelectronic and sensing applications.

## Acknowledgments

We thank Dongmao Zhang of the Department of Chemistry at Mississippi State University for helpful discussions and suggestions.

## Author Contributions

Conceptualization, C.W. and W.Z.; Methodology, C.W., X.Z. and Z.Y.; Validation, W.F.; Formal Analysis, C.W. and M.Z.; Data Curation, Z.Y.; Original Draft Preparation, C.W.; Review & Editing, W.Z.; Visualization, X.Z.; Supervision, Project Administration, and Funding Acquisition, W.Z.

## Ethics Statement

Not applicable.

## Informed Consent Statement

Not applicable.

## Data Availability Statement

All research data related to the paper are accessible and provided by the authors.

## Funding

This research was funded by [the Key Science and Technology Program of Kaifeng City] grant number [2301002].

## Declaration of Competing Interest

The authors declare that they have no known competing financial interests or personal relationships that could have appeared to influence the work reported in this paper.

## References

1. Miao P, Han K, Tang Y, Wang B, Lin T. Cheng W. Recent Advances in Carbon Nanodots: Synthesis, Properties and Biomedical Applications. *Nanoscale* **2015**, *7*, 1586–1595.
2. Koz K OE, Sudolsk MR, Pramanik G, Gler PC, Otyepka M, Zbo Il R. Photoluminescent Carbon Nanostructures. *Chem. Mater.* **2016**, *28*, 4085–4128.
3. Zhang W, Liu Y, Meng X, Ding T, Xu Y, Xu H, et al. Graphenol Defects Induced Blue Emission Enhancement in Chemically Reduced Graphene Quantum Dots. *Phys. Chem. Chem. Phys.* **2015**, *17*, 22361–22366.
4. Wang Y, Liu Y, Gao X, Zhan Y, Pan L, Zhang W, et al. Surface Defect Passivation of Graphene Quantum Dots by Amino Functionalization and Photoluminescence Emission Enhancement. *Acta Phys.-Chim. Sin.* **2016**, *32*, 2636–2644.
5. Zhang W, Wang Y, Liu X, Meng X, Xu H, Xu Y, et al. Insight into the Multiple Quasi-Molecular States in Ethylenediamine Reduced Graphene Nanodots. *Phys. Chem. Chem. Phys.* **2017**, *19*, 28653–28665.
6. Dong Y, Pang H, Yang HB, Guo C, Shao J, Chi Y, et al. Carbon-Based Dots Co-Doped with Nitrogen and Sulfur for High Quantum Yield and Excitation-Independent Emission. *Angew. Chem. Int. Edit.* **2013**, *52*, 7800–7804.
7. Zhang Y, Liu X, Fan Y, Guo X, Zhou L, Lv Y, et al. One-Step Microwave Synthesis of N-Doped Hydroxyl-Functionalized Carbon Dots with Ultra-High Fluorescence Quantum Yields. *Nanoscale* **2016**, *8*, 15281–15287.
8. Hu YP, Yang J, Tian JW, Yu JS. How Do Nitrogen-Doped Carbon Dots Generate from Molecular Precursors? An Investigation of the Formation Mechanism and a Solution-Based Large-Scale Synthesis. *J. Mater. Chem. B* **2015**, *3*, 5608–5614.
9. Khan S, Gupta A, Verma NC, Nandi CK. Time-Resolved Emission Reveals Ensemble of Emissive States as the Origin of Multicolor Fluorescence in Carbon Dots. *Nano Lett.* **2015**, *15*, 8300–8305.
10. Jiang K, Sun S, Zhang L, Lu Y, Wu A, Cai C, et al. Red, Green, and Blue Luminescence by Carbon Dots: Full-Color Emission Tuning and Multicolor Cellular Imaging. *Angew. Chem. Int. Edit.* **2015**, *54*, 5360–5363.
11. Nie H, Li M, Li Q, Liang S, Tan Y, Sheng L, et al. Carbon Dots with Continuously Tunable Full-Color Emission and their Application in Ratiometric pH Sensing. *Chem. Mater.* **2014**, *26*, 3104–3112.
12. Do S, Kwon W, Rhee SW. Soft-Template Synthesis of Nitrogen-Doped Carbon Nanodots: Tunable Visible-Light Photoluminescence and Phosphor-Based Light-Emitting Diodes. *J. Mater. Chem. C* **2014**, *2*, 4221.
13. Wu W, Zhan L, Fan W, Song J, Li X, Li Z, et al. Cu-N Dopants Boost Electron Transfer and Photooxidation Reactions of Carbon Dots. *Angew. Chem. Int. Edit.* **2015**, *54*, 6540–6544.
14. Wang S, Chen Z, Cole I, Li Q. Structural Evolution of Graphene Quantum Dots During Thermal Decomposition of Citric Acid and the Corresponding Photoluminescence. *Carbon* **2015**, *82*, 304–313.
15. Miao X, Qu D, Yang D, Nie B, Zhao Y, Fan H, et al. Synthesis of Carbon Dots with Multiple Color Emission by Controlled Graphitization and Surface Functionalization. *Adv. Mater.* **2018**, *30*, 1704740.
16. Liu YH, Duan WX, Song W, Liu JJ, Ren CL, Wu J, et al. Red Emission B, N, S-co-Doped Carbon Dots for Colorimetric and Fluorescent Dual Mode Detection of $Fe^{3+}$ Ions in Complex Biological Fluids and Living Cells. *ACS Appl. Mater. Inter.* **2017**, *9*, 12663–12672.
17. Wu MH, Zhan J, Geng BJ, He PP, Wu K, Wang L, et al. Scalable Synthesis of Organic-Soluble Carbon Quantum Dots: Superior Optical Properties in Solvents, Solids, and LEDs. *Nanoscale* **2017**, *9*, 13195–13202.
18. Hola K, Sudolska M, Kalytchuk S, Nachtigallova D, Rogach AL, Otyepka M, et al. Graphitic Nitrogen Triggers Red Fluorescence in Carbon Dots. *ACS Nano* **2017**, *11*, 12402–12410.
19. Wang ZF, Yuan FL, Li XH, Li YC, Zhong HZ, Fan LZ, et al. 53% Efficient Red Emissive Carbon Quantum Dots for High Color Rendering and Stable Warm White-Light-Emitting Diodes. *Adv. Mater.* **2017**, *29*, 1702910.
20. Liu C, Xiao GJ, Yang ML, Zou B, Zhang ZL, Pang DW. Mechanofluorochromic Carbon Nanodots: Controllable Pressure-Triggered Blue- and Red-Shifted Photoluminescence. *Angew. Chem. Int. Edit.* **2018**, *57*, 1893–1897.

21. Gao T, Wang X, Yang LY, He H, Ba XX, Zhao J, et al. Red, Yellow, and Blue Luminescence by Graphene Quantum Dots: Syntheses, Mechanism, and Cellular Imaging. *ACS Appl. Mater. Interfaces* **2017**, *9*, 24846–24856.
22. Miao X, Yan XL, Qu D, Li DB, Tao FF, Sun ZC. Red Emissive Sulfur, Nitrogen Codoped Carbon Dots and their Application in Ion Detection and Theranostics. *ACS Appl. Mater. Interfaces* **2017**, *9*, 25062–25062.
23. Zuo GC, Xie A, Li JJ, Su T, Pan XH, Dong W. Large Emission Red-Shift of Carbon Dots by Fluorine Doping and their Applications for Red Cell Imaging and Sensitive Intracellular $Ag^+$ Detection. *J. Phys. Chem. C* **2017**, *121*, 26558–26565.
24. Qu S, Zhou D, Li D, Ji W, Jing P, Han D, et al. Toward Efficient Orange Emissive Carbon Nanodots through Conjugated sp2-Domain Controlling and Surface Charges Engineering. *Adv. Mater.* **2016**, *28*, 3516–3521.
25. Fu M, Ehrat F, Wang Y, Milowska KZ, Reckmeier C, Rogach AL, et al. Carbon Dots: A Unique Fluorescent Cocktail of Polycyclic Aromatic Hydrocarbons. *Nano Lett.* **2015**, *15*, 6030–6035.
26. Strauss V, Margraf JT, Dolle C, Butz B, Nacken TJ, Walter J, et al. Carbon Nanodots: Toward a Comprehensive Understanding of their Photoluminescence. *J. Am. Chem. Soc.* **2014**, *136*, 17308–17316.
27. Chizhik AM, Stein S, Dekaliuk MO, Battle C, Li W, Huss A, et al. Super-Resolution Optical Fluctuation Bio-Imaging with Dual-Color Carbon Nanodots. *Nano Lett.* **2016**, *16*, 237–242.
28. Hu S, Trinchi A, Atkin P, Cole I. Tunable Photoluminescence Across the Entire Visible Spectrum from Carbon Dots Excited by White Light. *Angew. Chem. Int. Edit.* **2015**, *54*, 2970–2974.
29. Sciortino A, Marino E, Dam BV, Schall P, Cannas M, Messina F. Solvatochromism Unravels the Emission Mechanism of Carbon Nanodots. *J. Phys. Chem. Lett.* **2016**, *7*, 3419–3423.
30. Ding H, Yu S, Wei J, Xiong H. Full-Color Light-Emitting Carbon Dots with a Surface-State-Controlled Luminescence Mechanism. *ACS Nano* **2015**, *10*, 484–491.
31. Zhang TX, Zhu JY, Zhai Y, Wang H, Bai X, Dong B, et al. A Novel Mechanism for Red Emission Carbon Dots: Hydrogen Bond Dominated Molecular States Emission. *Nanoscale* **2017**, *9*, 13042–13051.
32. Righetto M, Privitera A, Fortunati I, Mosconi D, Zerbetto M, Curri ML, et al. Spectroscopic Insights into Carbon Dot Systems. *J. Phys. Chem. Lett.* **2017**, *8*, 2236–2242.
33. Essner JB, Kist JA, Polo-Parada L, Baker GA. Artifacts and Errors Associated with the Ubiquitous Presence of Fluorescent Impurities in Carbon Nanodots. *Chem. Mater.* **2018**, *30*, 1878–1887.
34. Shi L, Yang JH, Zeng HB, Chen YM, Yang SC, Wu C, et al. Carbon Dots with High Fluorescence Quantum Yield: The Fluorescence Originates from Organic Fluorophores. *Nanoscale* **2016**, *8*, 14374–14378.
35. Zhu SJ, Zhao XH, Song YB, Lu SY, Yang B. Beyond Bottom-Up Carbon Nanodots: Citric-Acid Derived Organic Molecules. *Nano Today* **2016**, *11*, 128–132.
36. Kasprzyk W, Świergosz T, Bednarz S, Walas K, Bashmakova NV, Bogdał D. Luminescence Phenomena of Carbon Dots Derived from Citric Acid and Urea—a Molecular Insight. *Nanoscale* **2018**, *10*, 13889–13894.
37. Kasprzyk W, Bednarz S, Żmudzki P, Galica M, Bogdał D. Novel Efficient Fluorophores Synthesized from Citric Acid. *RSC Adv.* **2015**, *5*, 34795–34799.
38. Krysmann MJ, Kelarakis A, Dallas P, Giannelis EP. Formation Mechanism of Carbogenic Nanoparticles with Dual Photoluminescence Emission. *J. Am. Chem. Soc.* **2012**, *134*, 747–750.
39. Liu X, Li H, Shi L, Meng X, Wang Y, Chen X, et al. Structure and Photoluminescence Evolution of Nanodots During Pyrolysis of Citric Acid: From Molecular Nanoclusters to Carbogenic Nanoparticles. *J. Mater. Chem. C* **2017**, *5*, 10302–10312.
40. Zhang J, Yang L, Yuan Y, Jiang J, Yu S. One-Pot Gram-Scale Synthesis of Nitrogen and Sulfur Embedded Organic Dots with Distinctive Fluorescence Behaviors in Free and Aggregated States. *Chem. Mater.* **2016**, *28*, 4367–4374.
41. Gude V, Das A, Chatterjee T, Mandal PK. Molecular Origin of Photoluminescence of Carbon Dots: Aggregation-Induced Orange-Red Emission. *Phys. Chem. Chem. Phys.* **2016**, *18*, 28274–28280.
42. Hu Q, Meng X, Chan W. An Investigation on the Chemical Structure of Nitrogen and Sulfur Codoped Carbon Nanoparticles by Ultra-Performance Liquid Chromatography-Tandem Mass Spectrometry. *Anal. Bioanal. Chem.* **2016**, *408*, 5347–5357.
43. Zhang W, Shi L, Liu Y, Meng X, Xu H, Xu Y, et al. Supramolecular Interactions Via Hydrogen Bonding Contributing to Citric-Acid Derived Carbon Dots with High Quantum Yield and Sensitive Photoluminescence. *RSC Adv.* **2017**, *7*, 20345–20353.
44. Meng X, Wang Y, Liu X, Wang M, Zhan Y, Liu Y, et al. Supramolecular Nanodots Derived from Citric Acid and Beta-Amines with High Quantum Yield and Sensitive Photoluminescence. *Opt. Mater.* **2018**, *77*, 48–54.
45. Sharma A, Gadly T, Gupta A, Ballal A, Ghosh SK, Kumbhakar M. Origin of Excitation Dependent Fluorescence in Carbon Nanodots. *J. Phys. Chem. Lett.* **2016**, *7*, 3695–3702.
46. Sharma A, Gadly T, Neogy S, Ghosh SK, Kumbhakar M. Molecular Origin and Self-Assembly of Fluorescent Carbon Nanodots in Polar Solvents. *J. Phys. Chem. Lett.* **2017**, *8*, 1044–1052.
47. Reckmeier CJ, Schneider J, Xiong Y, Häusler J, Kasák P, Schnick W, et al. Aggregated Molecular Fluorophores in the Ammonothermal Synthesis of Carbon Dots. *Chem. Mater.* **2017**, *29*, 10352–10361.
48. Xiao L, Wang Y, Huang Y, Wong T, Sun H. Self-Trapped Exciton Emission from Carbon Dots Investigated by Polarization Anisotropy of Photoluminescence and Photoexcitation. *Nanoscale* **2017**, *9*, 12637–12646.

49. Ghosh S, Chizhik AM, Karedla N, Dekaliuk MO, Gregor I, Schuhmann H, et al. Photoluminescence of Carbon Nanodots: Dipole Emission Centers and Electron—Phonon Coupling. *Nano Lett.* **2014**, *14*, 5656–5661.
50. Demchenko AP, Dekaliuk MO. The Origin of Emissive States of Carbon Nanoparticles Derived from Ensemble-Averaged and Single-Molecular Studies. *Nanoscale* **2016**, *8*, 1457–1469.
51. Malyukin Y, Viagin O, Maksimchuk P, Dekaliuk M, Demchenko A. Insight into the Mechanism of the Photoluminescence of Carbon Nanoparticles Derived from Cryogenic Studies. *Nanoscale* **2018**, *10*, 9320–9328.
52. Ru Y, Waterhouse GIN, Lu S. Aggregation in Carbon Dots. *Aggregate* **2022**, *3*, e296.
53. Yang H, Liu Y, Guo Z, Lei B, Zhuang J, Zhang X, et al. Hydrophobic Carbon Dots with Blue Dispersed Emission and Red Aggregation-Induced Emission. *Nat. Commun.* **2019**, *10*, 1789.
54. Wang J, Zheng J, Yang Y, Liu X, Qiu J, Tian Y. Tunable Full-Color Solid-State Fluorescent Carbon Dots for Light Emitting Diodes. *Carbon* **2022**, *190*, 22–31.
55. Deng L, Wang XL, Kuang Y, Wang C, Luo L, Wang F, et al. Development of Hydrophilicity Gradient Ultracentrifugation Method for Photoluminescence Investigation of Separated Non-Sedimental Carbon Dots. *Nano Res.* **2015**, *8*, 2810–2821.
56. Berlepsch HV, Böttcher C. H-Aggregates of an Indocyanine Cy5 Dye: Transition from Strong to Weak Molecular Coupling. *J. Phys. Chem. B* **2015**, *119*, 11900–11909.
57. Eisfeld A, Briggs JS. The J- and H-bands of Organic Dye Aggregates. *Chem. Phys.* **2006**, *324*, 376–384.
58. Würthner F, Kaiser TE, Saha-Möller CR. J-Aggregates: From Serendipitous Discovery to Supramolecular Engineering of Functional Dye Materials. *Angew. Chem. Int. Edit.* **2011**, *50*, 3376–3410.
59. Huang T, Wu T, Zhu Z, Zhao L, Ci H, Gao X, et al. Self-Assembly Facilitated and Visible Light-Driven Generation of Carbon Dots. *Chem. Commun.* **2018**, *54*, 5960–5963.
60. Li Y, Lin H, Luo C, Wang Y, Jiang C, Qi R, et al. Aggregation Induced Red Shift Emission of Phosphorus Doped Carbon Dots. *RSC Adv.* **2017**, *7*, 32225–32228.
61. Liu ZX, Wu ZL, Gao MX, Liu H, Huang CZ. Carbon Dots with Aggregation Induced Emission Enhancement for Visual Permittivity Detection. *Chem. Commun.* **2016**, *52*, 2063–2066.
62. Kasha M. Energy Transfer Mechanisms and the Molecular Exciton Model for Molecular Aggregates. *Radiat. Res.* **2012**, 178, AV27–AV34.
63. Spano FC, Silva C. H-and J-Aggregate Behavior in Polymeric Semiconductors. Annu. *Rev. Phys. Chem.* **2014**, *65*, 477–500.
64. Spano FC. The Spectral Signatures of Frenkel Polarons in H- and J-Aggregates. *Accounts Chem. Res.* **2010**, *43*, 429–439.